Anal. Chem. **2009,** *81,* 4482–4492

Scanning Ion Conductance Microscopy: a Model for Experimentally Realistic Conditions and Image Interpretation

Martin A. Edwards,[†,‡] Cara G. Williams,[†] Anna L. Whitworth,[†] and Patrick R. Unwin*[,†]

Department of Chemistry and MOAC Doctoral Training Centre, University of Warwick, Coventry CV4 7AL, U.K.

Scanning ion conductance microscopy (SICM) is a scanned probe microscopy technique in which the probe is a fine glass pipet filled with a contact (reference) electrode and an electrolyte solution. The current flow between the reference electrode and a second reference electrode positioned in bulk solution when the two electrodes are biased externally can be used as a feedback signal to maintain a constant separation between the tip and a surface during imaging. In usual practice the tip position is modulated over a small amplitude perpendicular to the surface, and the resulting alternating current (AC) is used as the feedback signal, although the direct current can also be used. A comprehensive model for the current response is reported. Laplace's equation has been solved for the electrolyte solution for a range of tip geometries, enabling the factors controlling the tip current to be identified. The approach developed is shown to represent an improvement over earlier semiempirical treatments. To explore the influence of surface topography on the (AC) current response, various surfaces have been considered, including a tip moved toward a planar surface (in the normal direction) and tips scanned over a pit and a step in the surface. The results have allowed a critical assessment of the SICM response as a means of probing surface topography. Features identified through simulation have been found in experiments through studies of two model substrates for which imaging results are reported. In typical experimental practice, the response of the SICM tip to surface features occurs over much greater lateral distances than the size of the pipet aperture.

Scanning electrochemical probe microscopies (SEPMs) have received much attention for the functional imaging of interfaces.[1−8] SEPMs work by moving a fine electrode probe in close proximity to an interface and, simultaneously, measuring and recording an electrochemical signal while the scan takes place. It is possible to build a 2-dimensional image from this signal, measured as a function of electrochemical probe position in a plane parallel to the interface. The probes for SEPMs may be either a solid ultramicroelectrode (UME) or a micro- or nanopipet containing an electrolyte solution and a wire electrode to provide a contact. Scanning electrochemical microscopy (SECM)[1−3,6,9] employs both types of probes and usually detects a species of interest via either diffusion-limited amperometry[9] or potentiometry.[10] In contrast, scanning ion conductance microscopy (SICM)[4,5] measures the conductivity between an electrode inside a micro- or nanopipet and an electrode placed in bulk solution. The conductivity may also be measured through impedance SECM measurements.[11−16] The measured quantity in SICM and many SECM imaging modes is the current; understanding how the current is affected by the probe geometry and physical situation is important for interpreting the signal in these microscopies. Considerable attention has been given to understanding the current response at the UME in SECM,[2,3,17−24] but there has been comparatively little work on

* To whom correspondence should be addressed. E-mail: p.r.unwin@warwick.ac.uk. Phone: +44(0) 2476 523 264. Fax: +44(0) 2476 524 112.

[†] Department of Chemistry.

[‡] MOAC Doctoral Training Centre.

(1) Edwards, M. A.; Martin, S.; Whitworth, A. L.; Macpherson, J. V.; Unwin, P. R. *Physiol. Meas.* **2006**, *27*, R63−R108.
(2) Wittstock, G.; Burchardt, M.; Pust, S. E.; Shen, Y.; Zhao, C. *Angew. Chem., Int. Ed.* **2007**, *46*, 1584–1617.
(3) Bard, A. J.; Mirkin, M. V. *Scanning Electrochemical Microscopy*; Marcel Dekker: New York, 2001.
(4) Hansma, P. K.; Drake, B.; Marti, O.; Gould, S. A.; Prater, C. B. *Science* **1989**, *243*, 641–643.
(5) Shevchuk, A. I.; Gorelik, J.; Harding, S. E.; Lab, M. J.; Klenerman, D.; Korchev, Y. E. *Biophys. J.* **2001**, *81*, 1759–1764.
(6) Amemiya, S.; Bard, A. J.; Fan, F.-R. F.; Mirkin, M. V.; Unwin, P. R. *Annu. Rev. Anal. Chem.* **2008**, *1*, 95–131.
(7) Kranz, C.; Friedbacher, G.; Mizaikoff, B. *Anal. Chem.* **2001**, *73*, 2491.
(8) Macpherson, J. V.; Unwin, P. R. *Anal. Chem.* **2000**, *72*, 276.
(9) Bard, A. J.; Fan, F. R. F.; Kwak, J.; Lev, O. *Anal. Chem.* **1989**, *61*, 132–138.
(10) Horrocks, B. R.; Mirkin, M. V.; Pierce, D. T.; Bard, A. J.; Nagy, G.; Toth, K. *Anal. Chem.* **1993**, *65*, 1213–1224.
(11) Ervin, E. N.; White, H. S.; Baker, L. A.; Martin, C. R. *Anal. Chem.* **2006**, *78*, 6535–6541.
(12) Alpuche-Aviles, M. A.; Wipf, D. O. *Anal. Chem.* **2001**, *73*, 4873–4881.
(13) Ervin, E. N.; White, H. S.; Baker, L. A. *Anal. Chem.* **2005**, *77*, 5564–5569.
(14) Katemann, B. B.; Inchauspe, C. G.; Castro, P. A.; Schulte, A.; Calvo, E. J.; Schuhmann, W. *Electrochim. Acta* **2003**, *48*, 1115–1121.
(15) Etienne, M.; Schulte, A.; Schuhmann, W. *Electrochem. Commun.* **2004**, *6*, 288–293.
(16) Horrocks, B. R.; Schmidtke, D.; Heller, A.; Bard, A. J. *Anal. Chem.* **1993**, *65*, 3605–3614.
(17) Fulian, Q.; Fisher, A. C.; Denuault, G. *J. Phys. Chem. B* **1999**, *103*, 4387–4392.
(18) Fulian, Q.; Fisher, A. C.; Denuault, G. *J. Phys. Chem. B* **1999**, *103*, 4393–4398.
(19) Kwak, J.; Bard, A. *J. Anal. Chem.* **1989**, *61*, 1221–1227.
(20) Ciani, I.; Burt, D. P.; Daniele, S.; Unwin, P. R. *J. Phys. Chem. B* **2004**, *108*, 3801–3809.
(21) Dobson, P. S.; Weaver, J. M. R.; Holder, M. N.; Unwin, P. R.; Macpherson, J. V. *Anal. Chem.* **2005**, *77*, 424–434.
(22) Amphlett, J. L.; Denuault, G. *J. Phys. Chem. B* **1998**, *102*, 9946–9951.
(23) Pierce, D. T.; Unwin, P. R.; Bard, A. *J. Anal. Chem.* **1992**, *64*, 1795–1804.
(24) Zoski, C. G.; Mirkin, M. V. *Anal. Chem.* **2002**, *74*, 1986–1992.

10.1021/ac900376w CCC: $40.75
Published on Web 04/30/2009

understanding the current response in SICM, even though the technique offers superior spatial resolution.[5,25]

SICM employs a feedback loop to maintain a constant distance between the pipet and the surface, so that the displacement of the scanning pipet normal to the sample during a scan represents the topography of the surface. The quantity used for feedback may be the direct current (DC),[4] or more successfully its derivative,[5] which is calculated by measuring the amplitude of the current oscillation (alternating current, AC) when the pipet position is modulated perpendicular to the surface. Clearly, understanding how the geometry of the pipet and the topography of the surface affect the current is important for the interpretation and analysis of images.

SICM-type pipets have also been used in other techniques. In hybrid SICM-scanning near field optical microscopy (SNOM),[26] an optical fiber within the pipet is maintained at a constant distance from the surface, providing the light source for SNOM. A pipet filled with fluorescently labeled DNA has been used for nanowriting, using the electric field created near the tip of the pipet to control DNA deposition.[27] A double-barreled micropipet, with an SICM-channel used as a distance sensor for an ion sensitive microelectrode employed in the second channel,[28] has facilitated scanning ion-selective potentiometric microscopy as a subtechnique of SECM.

Two models are available which describe the current at a micropipet electrode as a function of distance from a planar surface; both represent the physical situation by a number of resistors in series using an idealized pipet geometry.[28,29] Additionally, Ying and co-workers[30] used the finite element method to investigate the electric field inside a nanopipet in bulk solution. The current at the pipet was not of interest, nor did they consider the effect of a surface in proximity to the tip, because their work concerned the trapping of DNA dielectrophoretically in a nanopipet.[30] The goal of this paper is to assess the extent to which the models alluded to above are applicable in practice and to develop a more comprehensive model of SICM which lends itself to more realistic probe and substrate geometries. Comparison is made of the simulation results with the currently available models, and the effect of varying the pipet geometry is explored. Experimental data are presented which highlight the main features arising from the simulated results, demonstrating that the simulations are of direct practical relevance. In typical experimental practice, the lateral response of the SICM tip to surface features is much broader than the size of the pipet aperture, which has implications to the interpretation of surface topography from SICM imaging.

EXPERIMENTAL SECTION

Probe Preparation and Characterization. Pairs of near identical (as checked by scanning electron microscopy) micropipets of internal diameter 1−4 μm were pulled from capillaries of 1.2 mm outer diameter, 0.69 mm inner diameter borosilicate glass (Harvard Apparatus, U.K.), using a laser puller (Model P-2000, Sutter Instrument Co., Novato, CA) following procedures outlined in the user manual. From each pair of pipets pulled, one was used to approach a surface, while the other was characterized by a Supra55-VP field emission-scanning electron microscope (Zeiss). Pipets for imaging were backfilled with a solution of 0.1 M KCl (Fisher Scientific, U.K.) prepared using Milli-Q reagent grade water (Millipore Corp.). Both the internal and external electrodes were chloridized silver wires (Goodfellow Metals, Ltd., Cambridge, U.K.) of 125 μm diameter and 1 mm diameter, respectively.

Electrochemical Measurements. A micropipet was mounted perpendicular to the surface of interest, initially using micrometer-driven linear stages (Newport, 461-XYZ-M) for coarse positioning. Piezoelectric actuators, fitted with strain gauge sensors (Nanocube P-611.3S, Physik Instrumente, Germany), were used for fine positioning. These were controlled by an amplifier/servo (E-664 LVPZT, Physik Instrumente), operated in open loop mode. This, in turn, was controlled by signals from a digital to analog converter (DAC) card (Model no. NI-6731, National Instruments). Data were acquired using a data acquisition (DAQ) card (Model No. NI PCI-6143, National Instruments.). Both cards were installed in a PC running LabVIEW 7.1 software (National Instruments). All experimental measurements were made in a Faraday cage. Tip currents were converted to voltages using a home-built current follower prior to data acquisition. The data were acquired through self-written LabVIEW virtual instruments. For imaging experiments, the pipet was moved to discrete points in the plane parallel to the surface of interest, typically in a raster pattern. At each step the micropipet was allowed to settle before the current was measured and the DC and AC components extracted. Feedback was implemented through a proportional-integral control loop.

Atomic Force Microscopy (AFM) Imaging. AFM images were obtained in air using an AFM-3 equipped with a Nanoscope E controller (both Digital Instruments, Santa Barbara, CA), operating in contact mode.

Substrates. Two substrates were imaged: (i) a silicon oxide calibration grid with a "waffle" pattern of 5 μm pits with a 10 μm pitch and 180 nm pit depth, purchased from Digital Instruments; (ii) a substrate comprising 5 μm wide bands of 0.5 μm height with 20 μm pitch, which was fabricated using a mask aligner.

Finite Element Modeling. Modeling was performed on a Viglen Intel Core 2 Duo 2.4 GHz computer equipped with 4 GB of RAM running Windows XP 64 bit edition. The commercial finite element modeling package Comsol Multiphysics 3.3a (Comsol AB, Sweden), with the Matlab interface (Release 2006b) (The MathWorks, Cambridge, U.K.) was used for simulations. A minimum of 20000 triangular mesh elements (2D simulations) or 60000 tetrahedral mesh elements (3D simulations) were employed in the simulations. All elements were of the second-order Lagrangian type. Mesh resolution was defined to be greatest around the tip of the pipet, and also the edges of a pit/step in a surface (where modeled). Simulations with finer meshes and using an adaptive solver, which refined the mesh where the error was greatest, were completed (neither shown), to confirm the meshes used were sufficiently fine so as to not adversely affect the accuracy of the solution.

(25) Shevchuk, A. I.; Frolenkov, G. I.; Sánchez, D.; James, P. S.; Freedman, N.; Lab, M. J.; Jones, R.; Klenerman, D.; Korchev, Y. E. *Angew. Chem., Int. Ed.* **2006**, *45*, 2212–2216.

(26) Korchev, Y. E.; Raval, M.; Lab, M. J.; Gorelik, J.; Edwards, C. R. W.; Rayment, T.; Klenerman, D. *Biophys. J.* **2000**, *78*, 2675–2679.

(27) Bruckbauer, A.; Ying, L.; Rothery, A. M.; Zhou, D.; Shevchuk, A. I.; Abell, C.; Korchev, Y. E.; Klenerman, D. *J. Am. Chem. Soc.* **2002**, *124*, 8810–8811.

(28) Wei, C.; Bard, A. J.; Nagy, G.; Toth, K. *Anal. Chem.* **1995**, *67*, 1346–1356.

(29) Nitz, H.; Kamp, J.; Fuchs, H. *Probe Microsc.* **1998**, *1*, 187–200.

(30) Ying, L.; White, S. S.; Bruckbauer, A.; Meadows, L.; Korchev, Y. E.; Klenerman, D. *Biophys. J.* **2004**, *86*, 1018–1027.

THEORY AND SIMULATIONS

Geometric quantities used in the models and throughout this paper are as follows: r_e, radius of external electrode (measured from aperture outer edge); r_i, internal radius of the pipet tip; r_o, outer radius of the pipet tip; h, pipet height; d, pipet to surface separation; θ, pipet semiangle. The additional geometric parameter, RG, is defined to be the ratio of the outer and inner radii, r_o/r_i. Additionally, we shall use U to represent the applied potential and κ the conductance of the electrolyte. Throughout, we shall also use i_{DC} to represent the current to the electrode and i_{AC} to represent the oscillating component of the current, which arises from oscillation of the tip position normal to a surface.

Nitz and co-workers[29] developed a fully analytical model using three resistors to represent the resistance of the inner pipet, R_p, a distance dependent resistance, R_z, and a resistance of the electrolyte solution outside the pipet radius, R_r. R_z was subsequently separated into three further resistors. The resistance of each resistor was calculated from a set of assumed electric fields. The resistance of the pipet, R_p, was given by

$$R_p = \frac{1}{\kappa}\frac{h}{\pi \cdot r_{ie} \cdot r_i} \tag{1}$$

The final expression for the current, as a function of z, arrived at, after approximating one of the resistances further was

$$I(z) \approx I_{sat}\left(1 + \frac{{}^3/_2 \ln(r_o/r_i)\cdot r_{ie}\cdot r_i}{h\cdot d}\right)^{-1} \tag{2}$$

where

$$I_{sat} = \frac{U}{R_p} \tag{3}$$

The semianalytical model presented by Wei and co-workers[28] breaks the full resistance into two resistors; one for the resistance inside the pipet and the other for the solution outside. An analytical expression was obtained for the resistance inside the pipet, equivalent to eq 1, although formulated in terms of different geometric parameters. The external resistance was deduced from the fit of an analytical function to numerical simulations.[19] The resulting equations, for the change in resistance, $\Delta R(L)$, as a function of normalized height, $L = d/a$, eq 4 and eq 5, are

$$\Delta R(L) = R_t(L) - R_{t,\infty} \tag{4}$$

$$\Delta R(L)/R_{sol,\infty} = -0.708 + 1.5151/L + 0.6553\exp(-2.4035/L) \tag{5}$$

where $R_{sol,\infty}$ is the bulk solution resistance (resistance of the solution with the probe in bulk solution), $R_{t,\infty}$ is the total resistance in bulk, and $R_t(L)$ is the distance dependent, total resistance. The solution resistance, $R_{sol,\infty}$, is set as $R_{sol,\infty} = a/4\kappa$, which was calculated by Newman[31] to be the resistance to a conducting disk of radius a situated in an infinite, insulating plane, surrounded by a medium of uniform conductivity, κ. Equations 4 and 5, together with a version of eq 1 are rearranged to give the current as a function of normalized distance, $i(L)$,

$$i(L) = \frac{4\pi a r_0}{4L_p + \pi r_0(0.292 + 1.5151/L + 0.6553\exp(-2.4035/L)} \tag{6}$$

Dividing eq 6 by the limiting current as the distance tends to infinity, i_∞, results in

$$i(L)/i_\infty = \frac{4L_p + 0.9473\pi r_0}{4L_p + \pi r_0(0.292 + 1.5151/L + 0.6553\exp(-2.4035/L)} \tag{7}$$

For the model developed in this paper, we make a number of simplifying assumptions whose effects are negligible for the situations that concern us but which generate caveats in the conclusions drawn. First, as both contact electrodes are large in surface area and the electrode reaction is rapid, we ignore the effects of electrode charging and charge transfer resistance. We also choose to ignore the effect of any charge, and of the associated double layer, on the pipet wall. The reasons for this and the effects are discussed later. Additionally, the substrate above which the pipet is placed is modeled as a perfect insulator, passing no current and permitting no electric field across it.

A variety of geometries were simulated, as illustrated in Figure 1. These were chosen to be representative of some commonly found experimental geometries; while in no way exhaustive, they can be used intuitively to highlight the effects of various parameters encountered in SICM experiments.

2-D Model. When the pipet is perpendicular to a planar surface, the geometry of the problem displays axial symmetry; thus the 2-D geometry depicted in Figure 1a can be used. The reference electrode in bulk solution is sufficiently large relative to the pipet aperture that it presents no resistance. Consequently, the effect of the external electrode is distributed along edges 10 and 12. It is important to note that the current lines at long distance are a consequence of this idealization and should not be taken as representative of the real situation in this location; however, this does not affect the calculated resistance. Similarly, modeling the internal electrode as an arc of a circle (edge 11), does not influence the current. The full set of boundary conditions is defined in Table 1.

To calculate the current, Laplace's equation was first solved for the electrolyte solution. The axisymmetric cylindrical geometry of interest warrants the use of cylindrical polar coordinates, with the angular term omitted. Thus, choosing r and z to be the radial and axial coordinates, respectively, we have:

$$\nabla^2\Phi = \frac{\partial^2\Phi}{\partial r^2} + \frac{1}{r}\frac{\partial\Phi}{\partial r} + \frac{\partial^2\Phi}{\partial z^2} = 0 \tag{8}$$

where Φ is the potential. The current, i, is calculated by the integration of flux on the boundary representing the electrode, Ω, which is boundary 11 in Figure 1a

$$i = 2\pi\kappa\int_\Omega r\,\nabla\Phi\cdot\vec{n} \tag{9}$$

where $\vec{n}$ is the unit normal to the edge.

As eq 8 is linear, it is possible to obtain a solution in normalized coordinates. The pipet inner radius, r_i, is used to normalize the

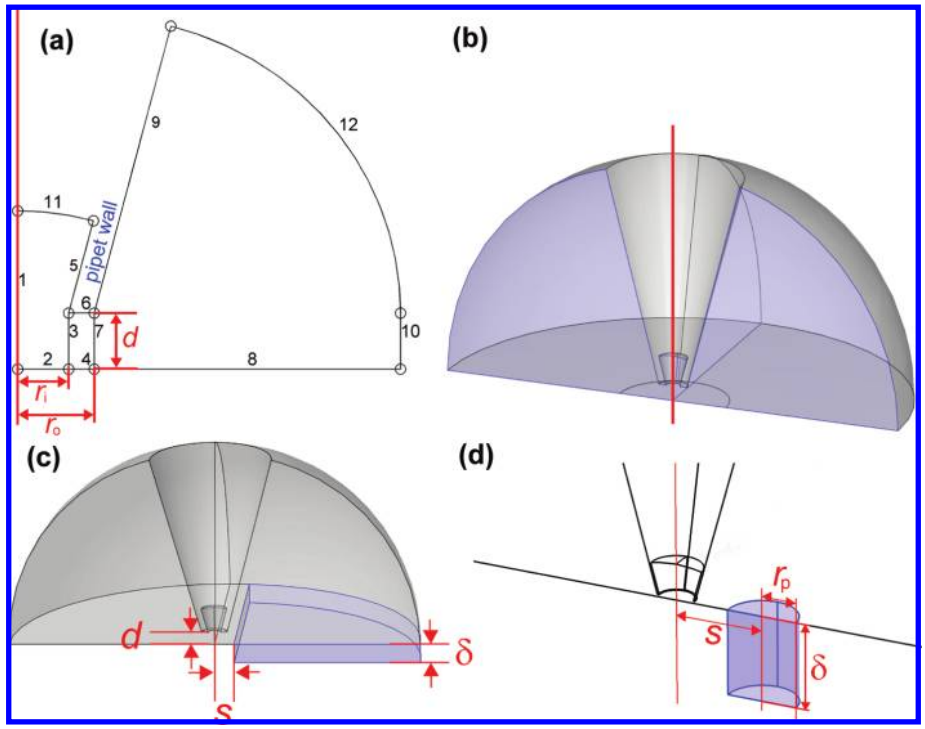

Figure 1. Geometries used for finite element simulations of (a) two-dimensional, cylindrically symmetric approach of an SICM tip to a planar surface; and three-dimensional simulation geometries for a tip above a planar surface (b), positioned near a step edge (c) and a cylindrical pit, zoomed to the region near the pipet end (d).

geometry. In addition, both the electrolyte conductivity, κ, and the potential, U, are taken to be unity, giving a general solution that may be scaled appropriately to match an experimental situation.

The length of the pipet is large compared to the pipet aperture, and although it would be possible to model the entire pipet this would be computationally inefficient. Greater efficiency in the simulations can be achieved by noting that the resistance, $R_{A,B,\gamma}$, between the conical segment of two concentric, spherical shells is

$$R_{A,B,\gamma} = \frac{B - A}{2\pi\kappa AB(1 - \cos(\gamma))} \tag{10}$$

where A and B are the radii of the outer and inner spheres respectively, γ is the semiangle of the conical section, and the other variables are as defined previously. Equation 10 is arrived at by first finding the potential distribution between two concentric shells, radii $A < B$, separated by a uniform medium of conductivity κ. The inner shell is poised at a potential of 0 V, while the outer shell is at 1 V. We describe the geometry of the system in spherical polar coordinates: r, ϕ, ψ; where r is the radial coordinate, ϕ is the azimuthal coordinate, and ψ is the polar coordinate. The symmetry of the system dictates that the solution will be independent of either angle; thus the equation solved is

$$0 = \nabla^2\Phi$$

$$= \frac{1}{r^2}\frac{\partial}{\partial r}\left(r^2\frac{\partial\Phi}{\partial r}\right) + \frac{1}{r^2\sin\theta}\frac{\partial}{\partial\theta}\left(\sin\theta\frac{\partial\Phi}{\partial\theta}\right) + \frac{1}{r^2\sin^2\theta}\frac{\partial^2\Phi}{\partial\theta^2}$$

$$= \frac{1}{r^2}\frac{\partial}{\partial r}\left(r^2\frac{\partial\Phi}{\partial r}\right) \tag{11}$$

The ansatz $\Phi(r,\phi,\theta) = \Phi(r) = \alpha + (\beta)/(r)$, with α, β constants to be determined, is made. Knowing the potential at the shells gives the simultaneous equations:

$$0 = \alpha + {}^{\beta}/_{A} \tag{12}$$

$$1 = \alpha + {}^{\beta}/_{B} \tag{13}$$

Solving eqs 12 and 13 gives

$$\alpha = B/(B - A) \quad \text{and} \quad \beta = AB/(B - A) \tag{14}$$

Through inspection we see the ansatz to be correct.

The current is calculated by integrating the normal flux $-\kappa\beta r^2$ over the portion of the inner shell lying within the bounds of the pipet ($\phi < \gamma$).

$$\text{Current} = \int_0^{2\pi}\int_0^{\gamma}(-\beta/A^2)\kappa A^2\sin\varphi \; \mathrm{d}\varphi \, \mathrm{d}\theta$$

$$= [AB/(B - A)]2\pi(1 - \cos\gamma) \tag{15}$$

The resistance is precisely the reciprocal of the current on application of a unit voltage, which is the relation of eq 15 to eq 10.

Equation 10 was used to calculate the resistance of the pipet from $2r_i$ upward, which was found through simulation to offer an accurate solution.

3-D Model. The starting geometry used in three-dimensional simulations was initially generated as the volume of rotation through 180° of the geometry shown in Figure 1a and described

Table 1. Boundary Conditions for the Simulations[a]

edge number	coordinates	physical representation	boundary condition
1	$r = 0; -d \le z \le h$	center-line of pipet	$\nabla\Phi\cdot\vec{n} = 0$
2	$z = -d; 0 < r < r_i$	inert surface	$\nabla\Phi\cdot\vec{n} = 0$
3	$r = r_i; -d < z < 0$	"phantom" boundary[b]	
4	$z = -d; r_i \le r \le r_o$	inert surface	$\nabla\Phi\cdot\vec{n} = 0$
5	$z = t\cos(\theta); r = r_i + t\sin(\theta); 0 \le t \le h$	pipet wall	$\nabla\Phi\cdot\vec{n} = 0$
6	$z = 0; r_i < r < r_o$	pipet wall	$\nabla\Phi\cdot\vec{n} = 0$
7	$r = r_o; -d < z < 0$	"phantom" boundary[b]	
8	$z = -d; r_o < r < r_o + r_e$	inert surface	$\nabla\Phi\cdot\vec{n} = 0$
9	$z = t\cos(\theta); r = r_o + t\sin(\theta); 0 < t < r_e$	pipet wall	$\nabla\Phi\cdot\vec{n} = 0$
10	$r = r_o + r_e; -d \le z \le 0$	external electrode	$\Phi = U = 1$
11	$r = (h + r_i/\tan(\theta))\sin(\varphi)$ $z = (h + r_i/\tan(\theta))\cos(\varphi) - r_i/\tan(\theta)$[c] $0 < \varphi < \theta$	internal electrode	$\Phi = 0$
12	$r = r_o + r_e\cos(\varphi)$ $z = r_e\sin(\varphi)$ $0 < \varphi < 90 - \theta$	external electrode	$\Phi = U = 1$

[a] The vector $\vec{n}$ is defined to be the unit normal to the boundary. [b] "Phantom" boundaries are introduced to aid the production of a high quality mesh but do not enforce a condition upon the solution. [c] These coordinates represent the arc of the circle whose center is the intersection of the extrapolation of the pipet center-line and the pipet inner wall.

in Table 1, giving the geometry shown in Figure 1b. Boundary conditions on the boundary surfaces were identical to those of the boundary lines of the 2-D model from which they arose. There is no longer a boundary condition applied on the axis of symmetry, which has been rotated about edge 1. The boundary shaded in blue in Figure 1b is the plane of symmetry for the simulation and, as such, has a "no flux" boundary condition applied to it, that is, $\nabla\Phi\cdot\vec{n} = 0$, where the vector $\vec{n}$ is defined to be the unit normal to the boundary plane. The partial differential equation solved was Laplace's equation in 3D Cartesian coordinates (x, y, z):

$$\nabla^2\Phi = \frac{\partial^2\Phi}{\partial x^2} + \frac{\partial^2\Phi}{\partial y^2} + \frac{\partial^2\Phi}{\partial z^2} = 0 \qquad (16)$$

The current, i, was calculated from eq 17, the analog to the flux integral described by eq 9, where Ω is now the boundary surface representative of one of the electrodes:

$$i = 2\kappa \int_{\Omega} \nabla\Phi\cdot n \qquad (17)$$

All equations were solved using the finite element method[32] which discretizes the problem as a series of polynomials on connected polyhedra. Initially, test simulations, for comparison with the two-dimensional formulation, were performed to confirm the validity of the mesh (not shown). Following this, two additional geometries, which cannot be represented in two dimensions, were considered: (i) the situation where the probe is scanned over a step (Figure 1c); and (ii) where the probe is scanned over a cylindrical pit (Figure 1d). In each case the shaded area in Figure 1c and d represents these additional features. The boundary conditions were "no flux" on all but the outer edge of the step domain, where the continuation of the outer hemisphere was given the condition $\Phi = U = 1$. Additional geometric parameters were introduced as follows: r_p is the pit radius; s represents the offset from the center-line of the pipet to the feature; δ represents the depth of the feature, be it a pit or a step. In the case of the step geometry, positive s refers to the case where the pipet is above the higher part of the step, as illustrated in Figure 1c. For the cylindrical pit case, there is a symmetry plane through the axis of the pit, and we make the arbitrary decision to only consider the case where s is non-negative. The perpendicular distance from the bottom end of the pipet to the upper part of the surface, as illustrated in Figure 1c, is denoted as d.

(31) Newman, J. *J. Electrochem. Soc.* **1966**, *113*, 501–502.
(32) Burnett, D. S., *Finite Element Analysis*; Addison-Wesley: Reading, MA, 1987.

RESULTS AND DISCUSSION

Factors Influencing SICM Approach Curves to a Planar Surface. Initially the effect of the micropipet semiangle on the current-distance response is considered. Figure 2a shows a set of current-distance curves for a micropipet of $RG = 1.1$ above a planar surface, for θ values of 3°, 5°, 10°, and 15°. It can be seen that increasing the pipet angle, θ, results in a steeper drop of normalized current as the tip is approached close to the surface. Thus, a tip with a small semiangle is, in essence, a less sensitive probe of tip-surface distance. The effect is easily understood in terms of the internal resistance of the pipets. The resistance of the pipet represents a large constant resistance in series with the resistance outside the pipet. The larger the resistance of the pipet (smaller the semiangle; see eq 10) the more dominant its contribution to the overall resistance, and the smaller the contribution from the remaining resistance (including distance-dependent resistance).

The effect of tip semiangle is further evident in Figure 2b, where the first harmonic (equivalent to the derivative) was calculated by differentiation of the normalized current, which was achieved by fitting a second-order interpolation polynomial through the simulated data points and differentiating this function. The first harmonic amplitude is zero far from the surface and increases more steeply with decreasing distance from the substrate (note the log scale on the graphs in Figure 2b). This contrasts with the DC signal (Figure 2a) where the current is large far from the surface and decreases only slowly (initially) with decreasing tip-substrate separation. Figure 2 shows clear evidence of the increased sensitivity afforded by using the first

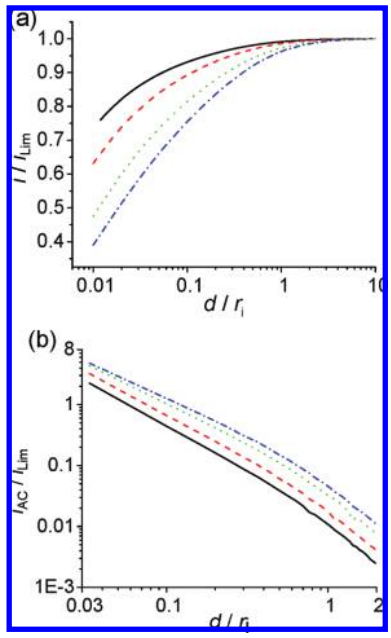

Figure 2. Simulated curves of the normalized current (a) and 1st harmonic (b), versus normalized distance, for the approach of $RG = 1.1$ micropipets, of varying semiangle, θ, to a planar inert surface. Solid black line, $\theta = 3°$; dashed red line, $\theta = 5°$; dotted green line, $\theta = 10°$; dash-dotted blue line, $\theta = 15°$.

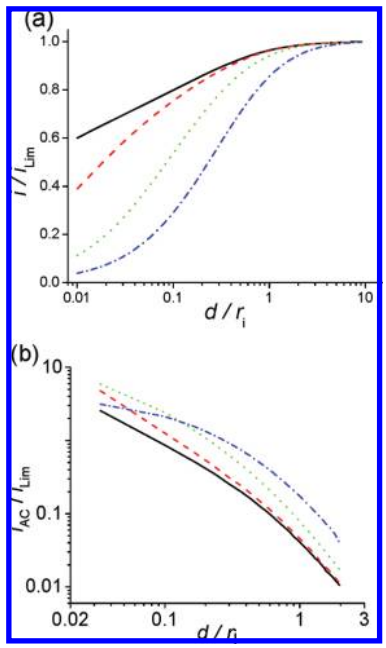

Figure 3. Simulation of the normalized current (a) and first harmonic (b), versus normalized distance, for the approach of 15° semiangle micropipets, of varying RG, to a planar inert surface. Solid black line, $RG = 1.01$; dashed red line, $RG = 1.1$; dotted green line, $RG = 2$; dash-dotted blue line, $RG = 10$.

harmonic as the feedback quantity, rather that the DC signal. Furthermore, the signal is largest with the larger θ value.

Figure 3a shows that the RG value has a similar effect on the sensitivity of the current response to distance as increasing the pipet semiangle, as is evident in the simulated current-distance curves for $\theta = 15°$, with $RG = 1.01$, 1.1, 2, and 10. It is important to note that although the distance-dependent currents shown in

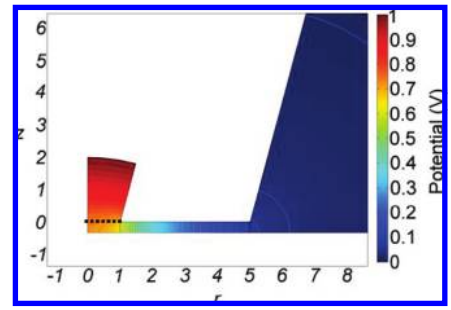

Figure 4. Plot of potential field of an $RG = 5$ tip near to a planar inert surface. Contours are isopotential lines (20 mV separation). Exterior only partially shown. Dashed black line denotes the tip aperture where previous treatments[28,29] have chosen to split the resistance.

Figure 3a are normalized by the bulk current for each particular pipet, the latter quantity only varies slightly with the RG value, with a decrease of just 3.3% from $RG = 1.01$ to $RG = 10$. This change under-represents the change in external resistance because of the large series resistance of the pipet interior, which contributes to the total resistance. It is clear that the increase in resistance with decreasing tip-substrate separation is much more significant with larger RG pipets. This trend is also evident in the plots of first harmonic normalized current versus distance shown in Figure 3b. The origin of the effect can be seen by inspection of Figure 4, which is a plot of the potential of the electric field around a tip of $RG = 5$. A significant potential drop, indicative of a high resistance, occurs in the annulus below the tip, bounded by the tip inner and outer radii. An increase in the size of this annulus necessarily increases the resistance and, consequently, the sensitivity of the tip response to distance from the surface. Examination of the isopotential contours in Figure 4 highlights that the aperture of the pipet (dashed line in the figure) is not an isopotential line; rather, the potential varies along it, as evident from the intersection of the dashed line with numerous isopotential contours. This means that splitting resistances along this line, as applied in previous treatments,[28,29] is not strictly correct. However, the variation of potential across the aperture is relatively minor and thus treating it as an equipotential line should only introduce limited error.

Effect of Substrate Topography. As discussed earlier, SICM imaging typically involves maintaining the first harmonic current signal of a probe oscillated perpendicularly to a surface of interest to maintain a constant tip-substrate separation as the tip is scanned across the surface.[5] Figure 5 shows simulations of the path tracked by a tip as it is scanned over a step in both AC and DC modes. The simulations were for a pipet geometry of $RG = 1.1$, with $\theta = 15°$, scanned over a step of height $\delta = 0.2r_i$, with feedback set-points of $d = 0.4r_i$, $d = 0.8r_i$ or $d = 1.1r_i$ [(a) and (c)]; or a step of height $\delta = r_i$ with feedback set-points of $d = 1.1r_i$, $d = 1.4r_i$ or $d = 1.7r_i$, [(b) and (d)]. Feedback control was achieved by maintaining the feedback quantity of either i_{AC} [(a) and (b)], or i_{DC} [(c) and (d)]. The height was solved for to give a tip-substrate separation where the feedback quantity attained the set-point value.

A schematic, illustrating the problem solved, is given in Figure 5e, together with the various parameters defining the problem. It can be seen that a step influences the tip position normal to the surface over relatively long lateral distances, and this effect

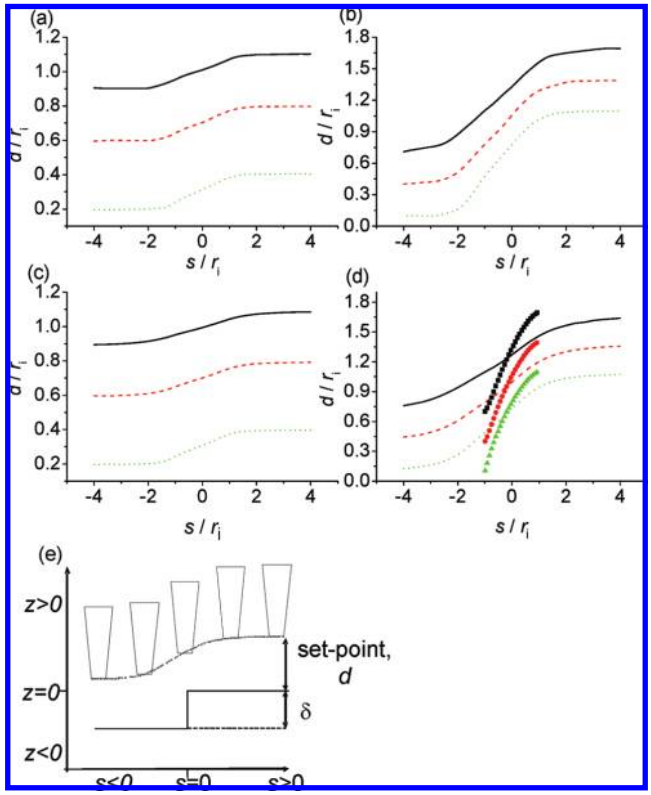

Figure 5. Profiles of tip height as a pipet (RG = 1.1, θ = 15°) is scanned over a step under feedback control. Lines in (a)−(d) are heights based on finite element simulations. The step height was: $\delta = 0.2r_i$ (a) and (c); and $1.0r_i$ (b) and (d). Feedback control considered: first harmonic (a) and (b); and the mean current (c) and (d). The lines shown in each plot represent different set-points: for (a) and (c) the solid black lines are $d = 1.1r_i$, dashed red lines, $d = 0.$ r_i, dotted green lines $d = 0.4$ r_i. For (b) and (d) the solid black lines are $d = 1.7r_i$, dashed red lines $d = 1.4r_i$, dotted green lines $d = 1.1r_i$. In part (d), the points represent the height of a pipet as it is scanned over a step ($\delta = 1r_i$) using feedback based on the mean current as calculated in Nitz et al.[29] to maintain the tip height with set-points defined by: black squares $1.7r_i$; red circles $1.4r_i$; green triangles $1.1r_i$. Part (e) summarizes the problem solved, with a schematic of the tip, together with the geometric parameters labeled.

becomes more extensive as the set-point is adjusted so as to move the imaging pipet further from the surface. Furthermore, it should be noted that the effect of the step does not result in a symmetric image profile. For example, in Figure 5b the tip begins to move perpendicularly to the surface at $s > 2r_i$ from the step, but reaches a plateau in less than $1.5r_i$ beyond the step. An important deduction from these results is that, the greater the height of the step and/or the tip set-point (distance from surface) the more blurred the feature will appear in an SICM image. For example, in Figure 5a, when the feedback set-point is at $d = 0.4r_i$ the pipet height traces out the step within a lateral distance of $\approx 2.9r_i$, whereas at a set-point of $d = 1.1r_i$ the response occurs over a greater lateral distance of $\approx 3.7r_i$. Comparing Figure 5a, for a step height of $\delta = 0.2r_i$, to Figure 5b for $\delta = r_i$, it can be seen that the large step is visible to the SICM probe, with equal set-points ($d = 1.1r_i$), over a marginally greater distance. It is interesting to note that, in practice, SICM typically operates with a set-point current corresponding to tip-substrate distances much greater than considered here.[5,25] At such distances, the

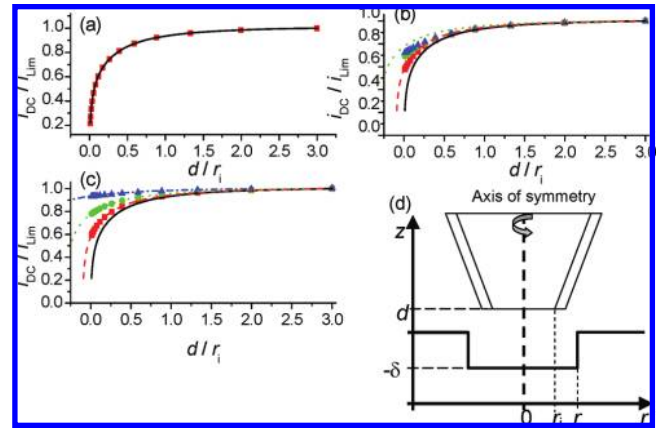

Figure 6. Steady-state current-distance curves as a pipet (RG = 1.1, θ = 15°) is approached to cylindrical pits (points in each plot) compared to the behavior for the same pipet approaching a planar surface (solid lines). Pit radii: $r_p = 0.73r_i$ (a); $r_p = 1.35r_i$ (b); and r_p = 5.74 r_i (c). Pipet and pit center-lines coincide ($s = 0$), that is, an axisymmetric cylindrical geometry is considered. Pit depths: red squares, $\delta = 0.1$ r_i; green circles $\delta = 0.31$ r_i; blue triangles, $\delta = 1$ r_i. Planar surfaces at heights: 0 r_i, solid black line; 0.1 r_i, dashed red line; 0.31 r_i, dotted green line; 1 r_i, dash-dotted blue line.

lateral response to surface features will be much broader than identified in this paper.

Figure 5c illustrates the probe scanning over the same step as Figure 5a, but the feedback quantity is i_{DC} rather than i_{AC}. The tip profile indicates that, compared to AC imaging, the use of the DC signal for feedback results in a broadening of the tip-height response curve. In the experiments reported later, and in present SICM practice,[5,25] i_{AC} has been selected for as the quantity for feedback to increase stability, as the AC signal is relatively immune to noise and drift, but the simulations reported herein also clearly demonstrate, for the first time, that AC feedback control yields a better tip response to surface features.

Figure 5d is the profile of a pipet scanned over a step $\delta = 1r_i$, while i_{DC} is maintained constant for feedback. The lines show tip heights for feedback set-points $d = 1.1r_i$, $d = 1.4r_i$, and $d = 1.7r_i$. The additional points on the plot represent the tip height for the same set-points, but using the current as calculated by Nitz et al.[29] for a tip scanning over a step. A dramatic difference in the results of the full simulation outlined herein and earlier work is evident and is an indication of the dangers of erroneous extrapolation of 2-dimensional results to 3 dimensions. The extrapolation method of Nitz et al.[29] takes the fraction of the pipet aperture over either side of the step to determine the fraction of the total current corresponding to a pipet at the equivalent distance from a planar surface. For example, a pipet r_i directly above a $\delta = 0.5r_i$ high step would have a current of $(i_{DC}(r_i) + i_{DC}(1.5r_i))/2$ to it. This method, which only takes into account features directly below the pipet, concludes that a complete response to the step would occur in a lateral distance equal to the pipet diameter ($2r_i$), regardless of the set-point or the height of the step. Our approach shows that this is incorrect because the method does not take into account lateral effects on the resistance.

Figure 6 summarizes the results of examining the effect of a pit in the substrate on the current response as a function of the

tip-substrate separation (pipet characterized by $RG = 1.1$, $\theta = 15°$). The following pit depths were considered: $\delta = 0.73r_i$ (a), $\delta = 1.35r_i$ (b), $\delta = 5.74r_i$ (c). In each case pit depths of $\delta = 0.1r_i$, $\delta = 0.31r_i$, and $\delta = 1r_i$ are considered and compared to a planar surface. In the cases shown, the tip and pit cylindrical axes of symmetry were coincident (2D simulation), as schematized in Figure 6d.

Figure 6a considers a set of pit depths for which the radius is slightly smaller than the pipet aperture ($r_p = 0.73r_i$). It is evident that the pits remains invisible to the tip when it is situated directly above, as indicated by the coincidence of all of the approach curves for the pits with the current-distance curve for a planar surface.

Figure 6b shows that when the pit is slightly larger than the pipet ($r_p = 1.35r_i$), the pit becomes visible to the tip, as indicated by a positive current deviation from the current-distance curve for a planar surface. However, only for the shallowest of pits ($\delta = 0.1r_i$) is the depth accurately assessed by SICM, that is, the current response is comparable to a pipet approaching a planar surface at $\delta = -0.1$. The lack of coincidence of the equivalent curves for deeper pits indicates that caution must be exercised when using SICM to infer the depth of pits of this radial scale compared to the tip.

Figure 6c demonstrates that for pits which are much larger radially than the pipet, for example, $r_p = 5.74r_i$, there is coincidence between the current response of a pipet approaching a pit and a planar surface of the same depth. We conclude that for pits of this size SICM measurements in the pit center are an accurate reflection of pit depth.

Figure 7 shows the simulated trajectory of a pipet as it is scanned over a cylindrical pit (depth $5r_i$; width r_p=$1.1r_i$ (a) and r_p=$2r_i$ (b) (for the geometry see Figure 1d and Figure 7c). The height was maintained using feedback on i_{AC} (feedback set-points $d = 0.35r_i$, $d = 0.45r_i$, $d = 0.6r_i$ (a); and $d = 0.8r_i$, $d = 1.1r_i$, $d = 1.4r_i$ (b)) as previously explained. The symmetry of the problem dictates that it is only necessary to display $s \geq 0$. It can be seen that the tip response to the pit overexaggerates the pit size, as evident from the height deviation, which extends far beyond the pit edge (indicated by the vertical lines in Figure 7a and b). This observation is consistent with that seen above the step feature. Additionally, as found for a pipet scanning over a step, the lateral response of the tip to the surface features becomes broader as the set-point distance from the surface increases. This can most readily be seen by comparing the curves in Figure 7b with feedback at $d = 0.8r_i$ and $d = 1.4\ r_i$. The larger set-point distance results in an increase of about r_i in the width of the height response traced out over the half-pit.

An important feature in Figure 7 is a dominant "halo" artifact: there is a decrease in tip height around the perimeter of the pit followed by an increase in height as the probe approaches the pit center, which would yield a halo in a 2-dimesional scan. To understand the origin of the "halo" artifact it is necessary to consider the ion paths in the vicinity of the tip, as illustrated schematically in Figure 8. When the tip is centered directly over the pit the only route for ion flow involves the narrow path between the pipet and surface (Figure 8a); however, if the pipet is off-center a second lower resistance path opens up, from the pipet via the pit to the exterior solution, as

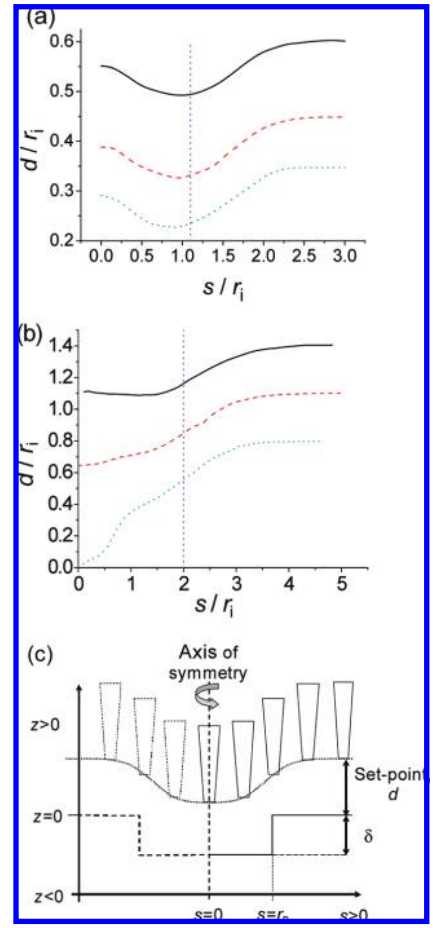

Figure 7. Profiles of tip height as a pipet ($RG = 1.1$, $\theta = 15°$) is scanned over a cylindrical pit of depth $\delta = 5\ r_i$. Pit radii were: $r_p = 1.1\ r_i$ (a) and $r_p = 2\ r_i$ (b). Vertical lines indicate the horizontal coordinate of the edge of the pit. Feedback control utilized the first harmonic, and the set-points were defined as distances from a planar surface as follows: solid black line $d = 0.6\ r_i$, dashed red line $d = 0.45r_i$, dotted green line $d = 0.35r_i$ (a); and solid black line $d = 1.4r_i$, dashed red line $d = 1.1r_i$, dotted green line $d = 0.8r_i$ (b). Part (c) is a schematic of the pit and tip with the geometric parameters labeled. This indicates that the scans in (a) and (b) start with the tip and pit coaxial and the tip is then moved radially outward.

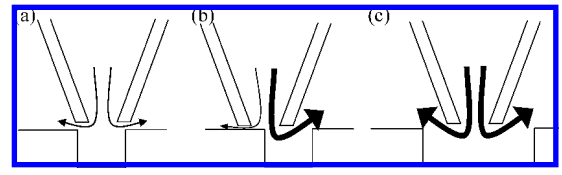

Figure 8. Schematic of the path of ion flow as a pipet is positioned above a pit either coaxially (a) or offset (b) over a small pit; or coaxially over a larger pit (c). The weight of the arrow is indicative of the relative magnitude of the ion flux out of the pipet. NB: there will be a net flow equal and opposite to balance the charge (not shown).

illustrated by the heavy arrow in Figure 8b. The artifact could also be viewed equivalently as an image of the tip aperture. It is clear that the artifact is no longer evident for the larger pit ($r_p = 2r_i$), that is, for the case where the glass aperture of the micropipet no longer encloses the entire pit (Figure 7b). However, for the closest feedback set-point ($d = 1.1r_i$), there is a second inflection at $s \approx 0.75r_i$, which corresponds to

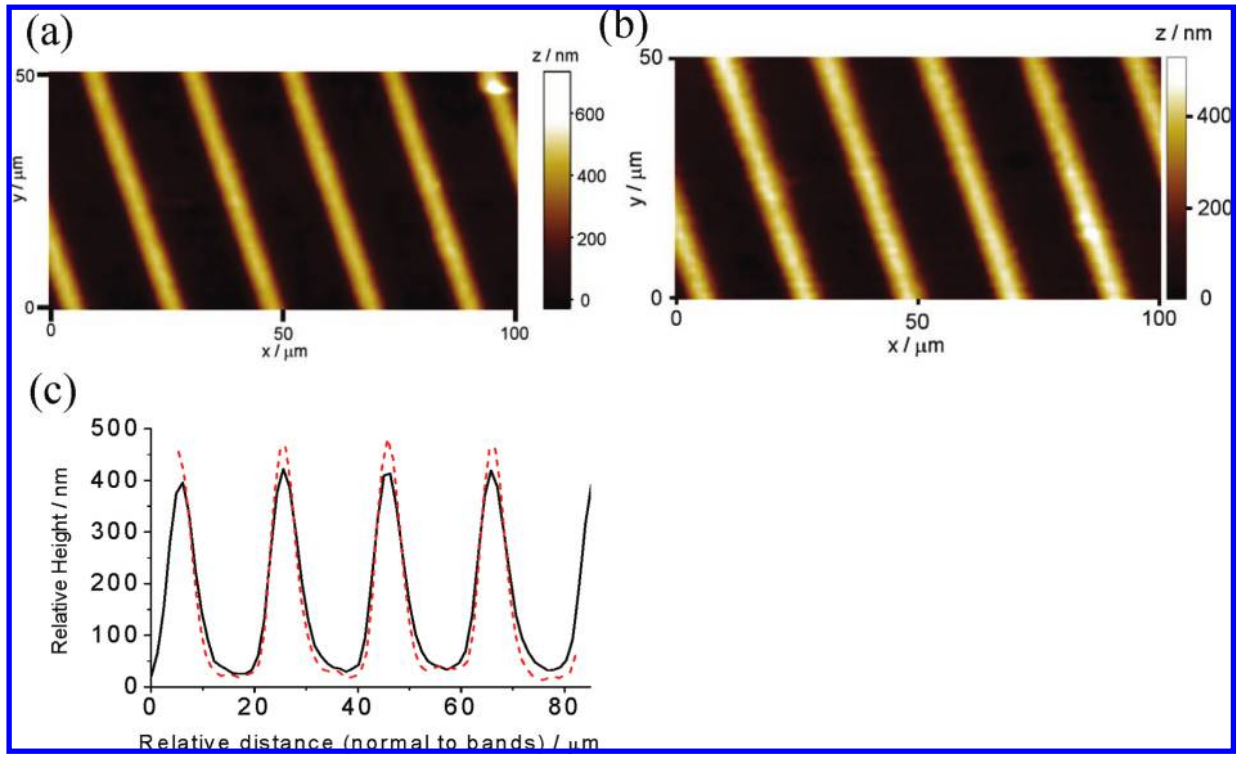

Figure 9. SICM image of raised band structure on silicon wafer, taken with a 3.5 μm inner diameter pipet under feedback utilizing the first harmonic, with two different set-points. The bandwidth was 5 μm, and the band height was 0.5 μm; 20 μm repeating pattern. (a) and (b) are images over the same 100 $\times$ 50 μm area, with set points of (a) $\approx$ 1.4*a*, and (b) $\approx$ 1.9*a*. Part (c) shows the average cross section in the direction normal to the bands for case (a) (dashed) and case (b) (solid). Lines have been shifted so that the flat areas between bands match approximately, so as to aid comparison. Imaging was performed at a sufficiently slow speed to ensure that the feedback was always at the set-point.

the pipet sidewall being within the region of the pit. In this situation there is an additional ion path of the type mentioned above and illustrated by the heavy arrow in Figure 8c.

Practical Assessment of SICM Tip Response. To examine the extent to which the characteristic features of SICM imaging, identified by simulation, were seen in practice, experiments were carried out on well-defined test samples. As an example, Figure 9 shows SICM images of a silicon sample comprising an array of 5 μm wide ridges of 0.5 μm height, with 20 μm pitch. The pipet used for imaging had an inner diameter of 3.5 μm, and the tip-substrate separation was achieved by maintaining the value of i_{AC} equivalent to the tip being close to the surface ($\approx$ 1.4*a*) (a) or further from the surface (b) ($\approx$ 1.9*a*). By comparing the data obtained with the different set-points, in both the images and in the cross-section plot shown in (c), it is clear that the topography response is a function of feedback set-point, although neither set-point was able to access the full height of the ridges. When the set-point places the tip closest to the surface (image (a)), the image is sharper (dashed line in Figure 9c), than for the more distant set-point (solid line Figure 9(c)). In both cases, the ridge was insufficiently wide compared to the tip to allow the tip profile to plateau at a height equal to the ridge thickness; however, the maximum height difference measured with the close set-point was greatest (400 nm cf. 350 nm with the bigger set-point).

All of the features observed in these experiments are consistent with the simulated results of a tip scanning over a step (Figure 5). The lack of a plateau in the tip height image over the center of the band is expected from the simulation results, which showed that a lateral distance equivalent to three or more tip radii beyond a step was required for a stable response to be attained. This condition is not achieved for a band of width about $3r_i$ as employed in the experiments. This factor in SICM imaging is further evident when one examines the part of the images corresponding to the flat portions between the bands. For the image where the set-point is closer to the surface, the flat portions are, in part, reproduced faithfully, but this is not the case where the set-point is further from the surface (see Figure 9c). The response for the latter case indicates that the tip detects the next step (band edge) before the influence of the previous one on the current response has ceased. The tip is thus unable to clearly identify the base features in the substrate topography. The midpoint between step edges is 7.5 μm, corresponding to a lateral distance of about $4r_i$. The simulated height profiles in Figure 5b show that when imaging close to the surface, a distance of $4r_i$ is sufficient for the tip to respond to a step change in the topography of the surface, but this lateral distance approaches the limit of that needed to observe the effect of a step.

Figure 10 shows images of a calibration grid taken with AFM (a) and SICM (c). For SICM imaging the internal diameter of the pipet was 1 μm and the tip-surface separation was achieved through maintaining the value of i_{AC} (set-point $\approx$1.2*a* from a planar surface). While the planar surfaces between the pits are clearly visible in the cross-section of the AFM image (b), these surfaces are clearly convoluted in the cross section of the SICM image (d); for the reasons discussed in connection with Figure 9. However, the depth at the center of the pits, measured with SICM ($\approx$ 170 nm), is in good agreement with the actual depths as quoted by the manufacturer (180 nm) demonstrating the quantitative nature of absolute height measurement with SICM.

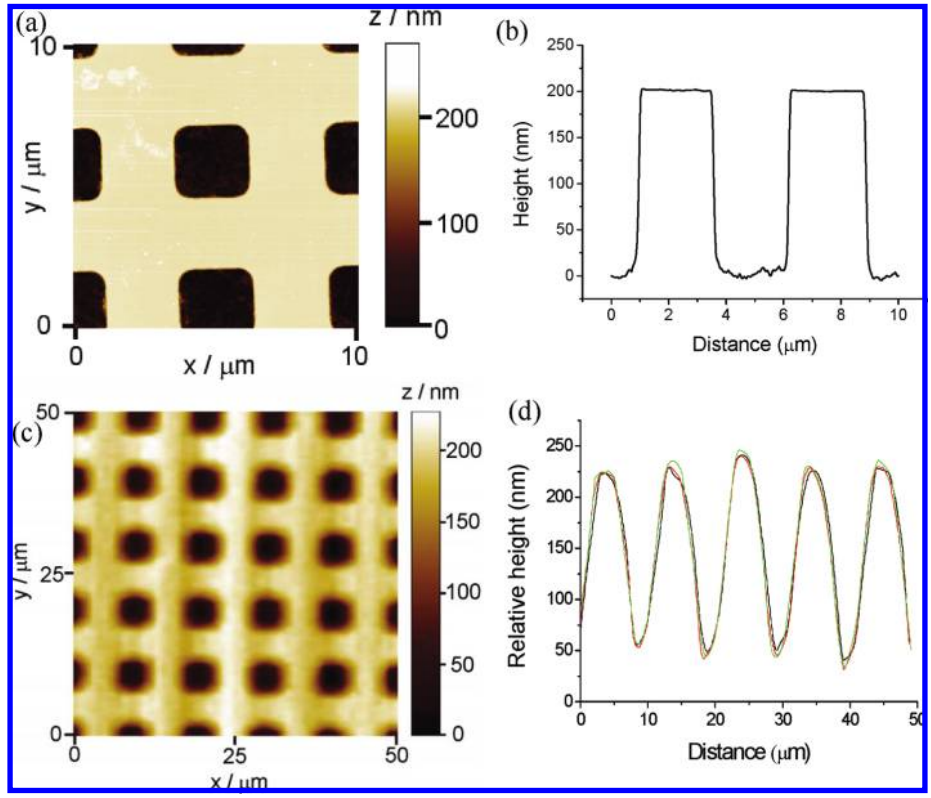

Figure 10. Images of a calibration grid, 10 μm pitch, 180 nm depth, taken with AFM (a) and (b); and SICM (1 μm internal diameter pipet, i_{AC} feedback, set-point $\approx$1.2*a*) (c) and (d). (b) and (d) are cross sections of the 2-dimensional images taken through the center of the pits, in (a) and (c), respectively. Curves in (d) have been aligned horizontally and vertically to aid comparison. Imaging was performed at a sufficiently slow speed to ensure that the feedback was always at the set-point.

Convolutions of the surface topography by an imaging method can in theory be reversed by an appropriate treatment, assuming one knows the response of the imaging method. However, as shown in this paper, the tip-height response to topography is complicated, relying on the solution of the Laplace equation. Deconvolution based on geometric exclusion, as is done in AFM,[33] would be inappropriate. Earlier work has examined improving the resolution of scanning electrochemical microscopy (SECM) by digital image processing.[34] The method relied on assuming the image response to be a Laplacian based blurring and an empirical choice of parameters, which gave "improved" images. To the authors' knowledge this work has not been continued. As SECM also relies on the solution of the Laplace equation (in this case relating to diffusion) it might be possible to apply a similar methodology to SICM images, although the challenge of empirical parameter selection would still remain.

CONCLUSIONS

Finite element modeling has enabled the current response of an electrolyte-filled SICM micropipet approaching a planar surface to be investigated as a function of the pipet geometry. The model represents an improvement and extension of previous attempts to study this problem.[28,29] We have demonstrated that a larger pipet semiangle and a larger ratio of glass to aperture radii (RG value) make SICM more sensitive to tip-sample separation.

To explore surface topography in SICM, the current responses have been investigated for a pipet scanned as follows: (i) toward a pit in the normal direction (axisymmetric geometry); and (ii) laterally over a step and across the mouth of a cylindrical pit. An instantaneous step in a surface is shown to be significantly convoluted to a feature typically influencing the image (tip response) over approximately four tip radii with the response being dependent on the tip/surface separation; close tip/surface separation improves the tip-height response to surface features. The responses reported herein should be considered as best case scenarios as, in practice, and with very small pipets, the tip to surface separation is typically greater than considered in this paper.[5,25] The lateral resolution of the technique has a strong dependence on the choice of feedback quantity, with the first harmonic offering a significantly improved lateral tip response when compared with the mean current. The ability to judge the depth of pits has shown to be dependent on the pit width, with only wide pits, with respect to the tip aperture, generally accessible.

It is important to point out that the model treats the experimental situation as a homogeneous, resistive medium, with the pipet walls and inert substrate surface both infinitely resistive. The homogeneity condition will break down if there is a concentration source, for example, a surface reaction, in which case a Nernst−Planck model, which considers diffusion acting on concentration gradients as well as migration of ions, must be used. If the electrolyte concentration is very low, or the pipet very small, then the size of the double layer on the glass will be significant

(33) Villarrubia, J. *J. Res. Natl. Inst. Stand. Technol.* **1997**, *102*, 425.
(34) Lee, C.; Wipf, D. O.; Bard, A. J.; Bartels, K.; Bovik, A. C. *Anal. Chem.* **1991**, *63*, 2442–2447.

as charge separation occurs; this case is not covered by the model presented, but could readily be considered in the future. The resulting permselectivity of the pipet would be reflected in a nonlinear current−voltage response, so-called current rectification, which has been considered for pipets in bulk solution.[35−38] In such conditions or with very high electric fields it may also be prudent to include electro-osmotic flow within the model.

The geometry of the pipet used in the modeling is a simplification of the experimental geometry; typically a pipet barrel may exhibit multiple tapers along its length. However, the resistance is concentrated at the tip of the pipet and its immediate exterior; thus in modeling this region accurately, we give a very accurate approximation to the response of the full pipet geometry. Although, in practice, the pipet is oscillated with a small amplitude perpendicular to the surface to obtain the first harmonic current signal, no attempt has been made to model the fluid flow associated or the transient effects as the electric field is developed. These simplifications are supported by experiments showing excellent agreement between the derivative of the current upon approach to a surface and the first harmonic on approach of the same pipet to the same surface, as has been shown previously.[5] The assumption of no charge transfer resistance is sound assuming care is taken to produce good reference electrodes for employment experimentally.

(35) Wei, C.; Bard, A. J.; Feldberg, S. W. *Anal. Chem.* **1997**, *69*, 4627–4633.
(36) Vlassiouk, I.; Siwy, Z. S. *Nano Lett.* **2007**, *7*, 552–556.
(37) Woermann, D. *Phys. Chem. Chem. Phys.* **2003**, *9*, 1853–1858.
(38) White, H. S.; Bund, A. *Langmuir* **2008**, *24*, 2212–2218.

Experimentally, the first harmonic is obtained through lock-in amplification; the mathematical equivalent of this operation being

$$2f\int_0^{1/f} i\left(d + \frac{\delta}{2}\sin(2\pi ft)\right)\sin(2\pi ft)\,dt \qquad (18)$$

where $i(-)$ is the current as a function of height. The first harmonic is thus a function of oscillation amplitude, which as δ diminishes tends to $\delta(\partial i(h))/(\partial h)|_{h=d}$. Upon normalization by the oscillation amplitude it leaves us with the derivative at the midpoint of oscillation. The equivalence taken between derivative and normalized first harmonic is thus entirely correct for low oscillation amplitudes. However, with large amplitude oscillation eq 18 should be evaluated to give the first-harmonic amplitude. With large amplitude oscillation some difference may be seen from the approach curves and tip trajectories shown in this paper.

ACKNOWLEDGMENT

This work was supported by EPSRC (MOAC/DTC studentship for M.A.E.) and GlaxoSmithKline (funding for C.G.W.), to whom we are grateful. A.L.W. thanks the Royal Society for support via a Dorothy Hodgkin-BP fellowship. We are grateful to Professor Julie Macpherson for helpful advice.

Received for review February 18, 2009. Accepted April 3, 2009.

AC900376W